Electronic Supplementary Information (ESI)

Electrospinning-Assisted Porous Skeleton Electrolytes for Semi-Solid Li-O$_2$ Batteries

Jing Wu[a], Minghui Li[a], Shasha Gao[b], Yaying Dou[a], Kecheng Pan[a], Zhang Zhang[a*], Zhen Zhou[a]

[a] Interdisciplinary Research Center for Sustainable Energy Science and Engineering (IRC4SE2), School of Chemical Engineering, Zhengzhou University, Zhengzhou 450001, China.

[b] Key Laboratory of Microelectronics and Energy of Henan Province, Department of Physics and Electronic Engineering, Xinyang Normal University, Xinyang 464000, China.

Experimental Section

Materials

Polyacrylonitrile (PAN; Mw = 150 000 g mol^{-1}, Aladdin), ruthenium (III) chloride hydrate (RuCl$_3$·xH$_2$O; Aladdin), multi-walled nanotubes (CNTs; Aladdin), polyvinylidene fluoride (PVDF; 99%, Thermo Fisher Scientific, Shanghai, China), bis(tri-fluorosulfonyl)imide lithium salt (LiTFSI; 99%, Aladdin), N,N-dimethylformamide (DMF; Aladdin, 99%), Tetraethyleneglycol dimethyl ether (TEGDME; 99%, Aladdin), N-methyl-2-pyrrolidinone (NMP; 99%, Aladdin).

Preparation of E-PLT Membrane

0.5 g of PAN was added into 4.5 g of DMF and stirred for 12 h. Subsequently, the precursor solution was inhaled into a syringe with a single stainless-steel nozzle for electrospinning. The power supply was maintained at 18 kV between the spinneret and the aluminum foil collector at a distance of 20 cm. The feeding rate of the pump was set to 0.01 mL s^{-1}, and the humidity of the preparation process was kept below 30%. The resulting electrospun film was then vacuum dried at 80 °C to remove residual solvents to obtain E-PAN films. The E-PAN membrane was soaked in the 10 μL 1.0 M LiTFSI/TEGDME liquid electrolyte for fully absorption and gelation to obtain E-PLT electrolyte.

Preparation of C-PAN Membrane

0.5 g of PAN was added into 4.5 g of DMF and stirred for 12 h. Dense membranes were prepared by solution-casting solutions on clean glass plates using a doctor blade. The resulting film was then vacuum dried at 80 °C to remove residual solvents to obtain C-PAN films. The C-PAN membrane was soaked in the 10 μL 1.0 M LiTFSI/TEGDME liquid electrolyte for fully absorption and gelation to obtain C-PLT electrolyte.

Preparation of RuO$_2$/CNT

RuO$_2$/CNT were synthesized according to the previously reported method.[1] 150 mg of CNTs and 200 mg of ruthenium (III) chloride hydrate (RuCl$_3$·H$_2$O) were dissolved in 40 mL of deionized water. The mixture was stirred for 12 hours until complete dissolution. The mixture was then transferred to a Teflon-lined stainless-steel

autoclave, sealed and kept at 150 °C for 5 h. The resulting samples were then centrifuged, dried and then calcined in air at 400 °C for 2 h to obtain RuO_2/CNT powder.

Battery assembly

The cathode was prepared by mixing RuO_2/CNT powder and PVDF with a weight ratio of 6:1 in N-methyl-2-pyrrolidone and casting on to carbon paper. The electrodes were dried at 100 °C in vacuum overnight. Prior to the battery assembly, lithium foil and carbon cathode were cut to discs with diameters of 14 and 12 mm, respectively. The Li/Li symmetric cell was assembled with the electrolyte membranes and tested at room temperature. The full cell was assembled using Li metal anode, C-PLT or E-PLT gel polymer electrolyte and RuO_2/CNT cathode. The non-aqueous $Li-O_2$ batteries were fabricated with Li metal anodes, liquid electrolytes (1 M LiTFSI/TEGDME, 100 µL) impregnated into glass fiber (GF) separators (Whatman), and RuO_2/CNT cathodes. All the batteries were assembled by using CR-2032 coin-type cell in an argon-filled glove box (H_2O, O_2 < 0.1 ppm) and further to test the electrochemical performances.

Electrochemical measurements

The ionic conductivities of electrolytes were measured by electrochemical impedance spectroscopy (EIS) of SS/electrolyte/SS blocking cell from 1 MHz to 0.1 Hz at temperature range of 20-100 °C. The ionic conductivity was calculated based on eq 1:

$$\sigma = \frac{L}{RS}$$

where L represents the thickness of the electrolyte membrane, R is obtained from the EIS measurements of the SS/electrolyte/SS blocking cells, and S is the effective contact area between the SS and the electrolyte membrane. The activation energy Ea was calculated according to Arrhenius equation on eq 2:

$$\sigma(T) = A exp\left(\frac{-E_a}{RT}\right)$$

where σ is the ionic conductivity of the electrolyte, A is a pre-exponential factor, Ea is the activation energy, and T is absolute temperature. The lithium-ion transference number (t_{Li^+}) was tested by chronoamperometry in the Li/Li symmetric cell and calculated basing on eq3:

$$t_{Li^+} = \frac{I_S}{I_0} \times \frac{(\Delta V - I_0 R_0)}{(\Delta V - I_S R_S)}$$

where ΔV is the polarization voltage applied (10 mV), I_0 and R_0 represent the initial current and resistance respectively, and I_S and R_S are the steady-state current and resistance after polarization, respectively. Electrochemical stability was tested by Linecsweep voltammetry (LSV) using SS/electrolyte/Li cells sweeping from 0 to 6 V at a constantrate of 0.1 mV s^{-1} were tested on a Solartron 1470E electrochemical workstation (1470E; Solartron Metrology, UK). The galvanostatic discharge/charge tests of $Li-O_2$ cells were performed on LAND CT3002A testers (CT3002A; LAND, Wuhan, China) in a pure O_2 glove box (H_2O < 0.1 ppm).

Materials characterization

The X-ray diffraction (XRD) patterns of the as-obtained samples were obtained using an Ultima IV X-ray diffractometer (Ultima IV, Rigaku, Japan) with Cu Kα radiation. Field emission scanning electron microscopy (SEM) was conducted using a JSM-6390 microscope from JEOL. X-ray photoelectron spectroscopy (XPS) was collected by using a Thermo ESCALAB 250 instrument with a monochromated Al X-ray resource at 1486.6 eV. Morphologies of samples were studied by using FESEM (Hitachi S-4800) and TEM (Hitachi H-600). The mechanical properties of electrolyte membranes were tested using a electronic universal testing machine（INSTRON 5982）. Thermal analysis was performed through thermogravimetric (TGA) with a TGA 550 under N_2 atmosphere from room temperature to 800 °C with a heating rate of 10 °C min^{-1}. Simultaneous thermal analyzer (HITACHI STA200) was used to conduct the differential scanning calorimetry under N_2 atmosphere from 100 °C to 400 °C at the heating rate of 10 °C min^{-1}.
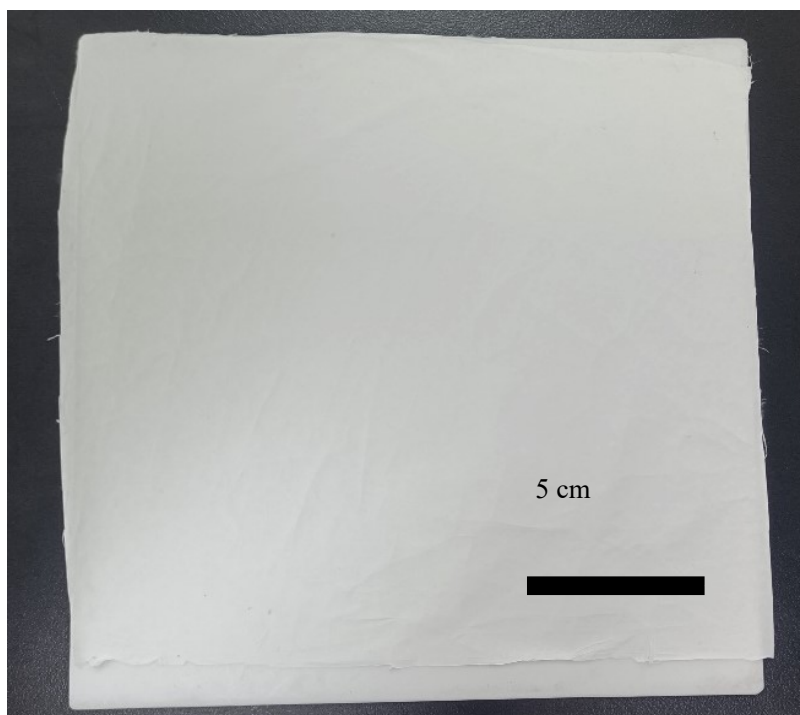
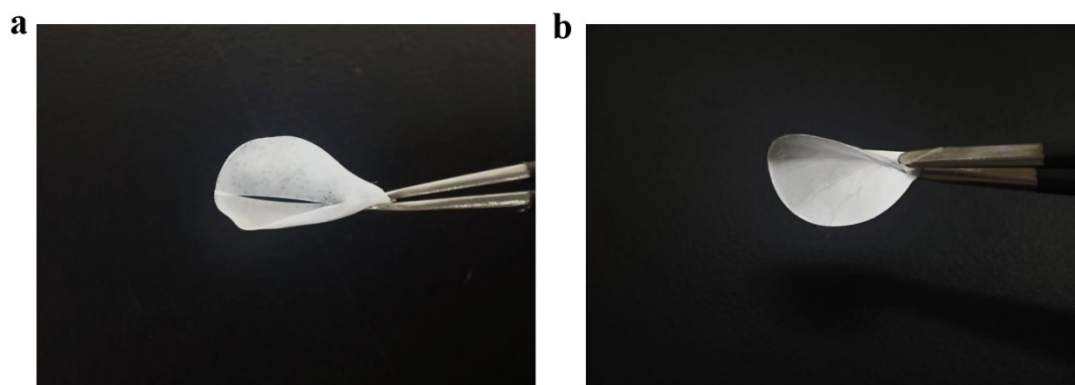**Figure S1.** Photo image of a nanofibrous PAN film.

Figure S2. Photo images of (a) C-PAN and (b) E-PAN membrane after 90° bending.

Folding the C-PAN membrane at a 90° angle resulted in cracking and compromised structural integrity, whereas the E-PAN membrane remained intact under the same conditions, indicating superior flexibility of membranes produced by electrostatic spinning compared with conventional solution casting.
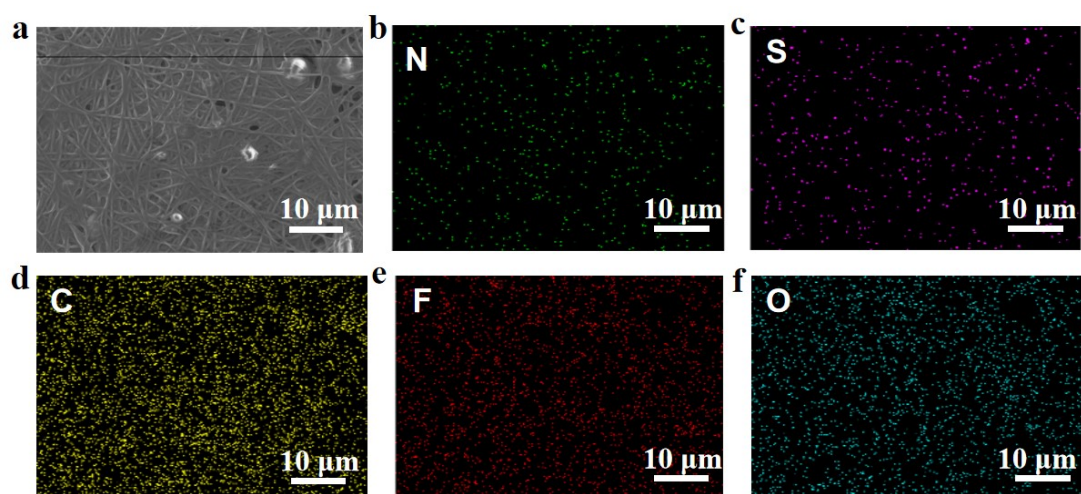

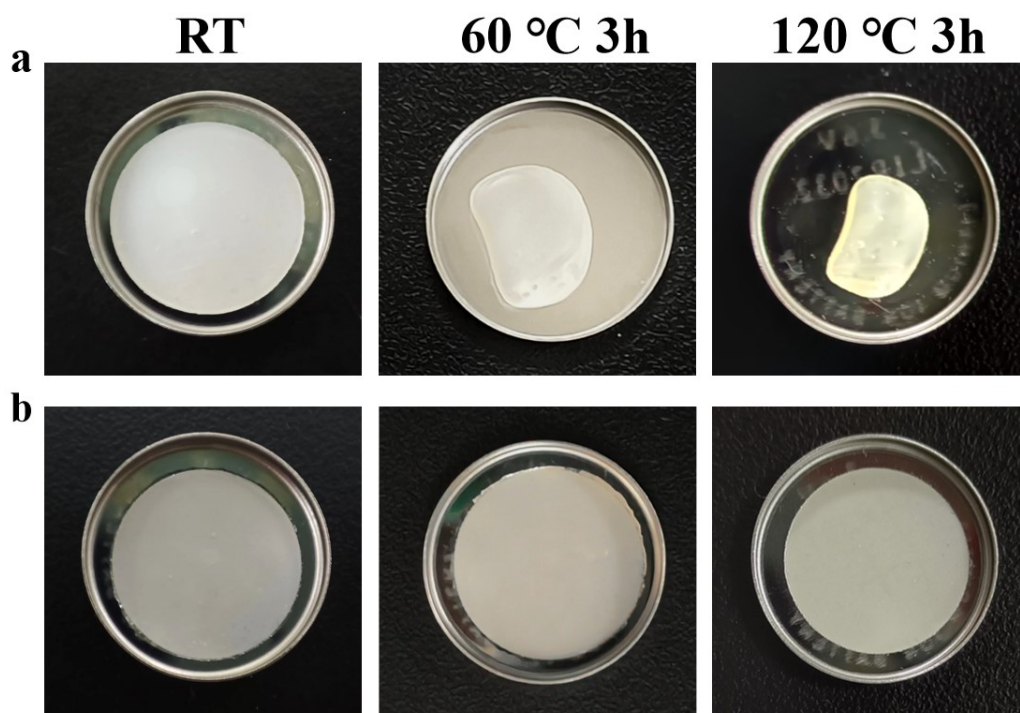**Figure S3.** SEM and corresponding EDS elemental mapping images of E-PLT.

Figure S4. Photo images of (a) C-PLT membrane and (b) E-PLT membrane before/after exposure to thermal shock at 60 °C for 3 h and 120 °C for 3 h.

Thermal shrinkage properties were examined by subjecting the membranes to heat treatment at different temperatures for 180 minutes. The C-PLT membrane experienced shrinkage at 60 °C, while the dimension and morphology of the E-PLT membrane remained unchanged at 120 °C, demonstrating excellent stability and deformation resistance at high temperatures.
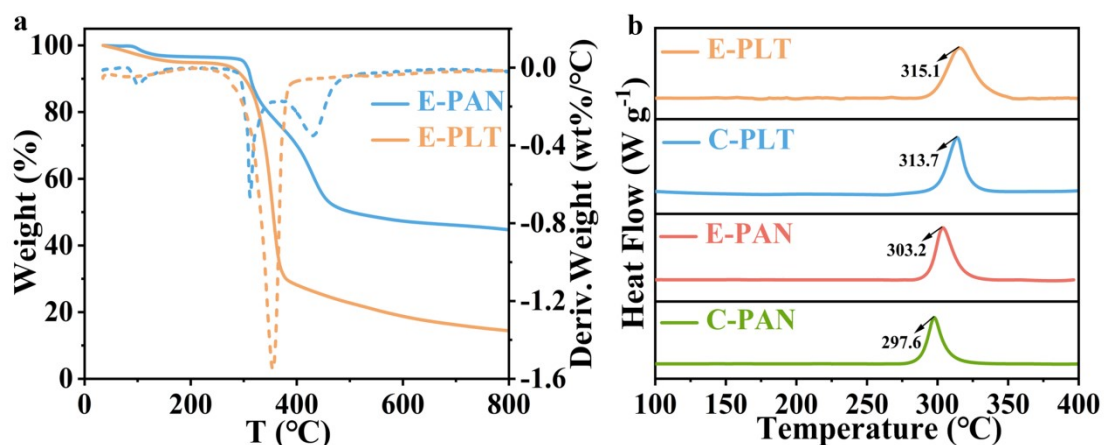
Figure S5. (a) TGA and DTG curves of E-PAN and E-PLT electrolyte. (b) DSC curves of C-PAN, E-PAN, C-PLT and E-PLT polymer membranes.

Further characterization reveals the excellent thermal stability of the polymer membrane. Thermogravimetric analysis (TGA) and differential thermogravimetry (DTG) showed only a marginal mass loss of 5% before reaching 200 °C for the E-PLT membrane, with exceptional thermal stability sustained up to 280 °C (Figure S5a). Furthermore, the thermal stability of the material was further confirmed using differential scanning calorimetry (DSC, Figure S5b). The decomposition onset temperatures corresponding to the exothermic peaks of E-PAN and E-PLT membranes are 303.2 °C and 315.1 °C, respectively. This indicates that both E-PAN and E-PLT membranes exhibit high thermal stability.
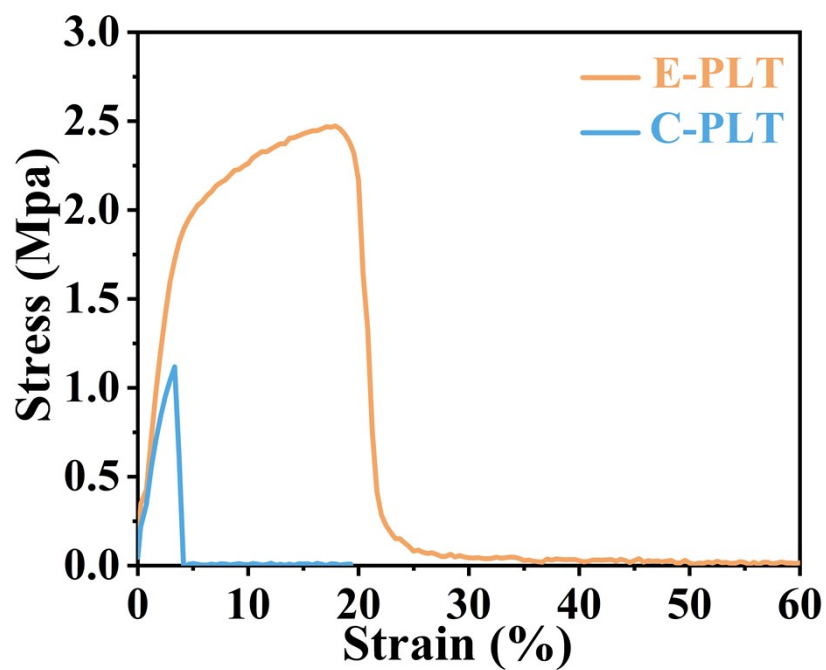
Figure S6. Stress-strain curves of C-PLT and E-PLT electrolyte during a tensile test.

Assessing the mechanical stability through stress-strain curves is crucial for ensuring the safety of the battery. The stress-strain curve revealing a tensile stress of 2.47 MPa and an elongation at break of approximately 27.5% for the E-PLT membrane, surpassing the mechanical performance of the C-PLT fiber membrane.
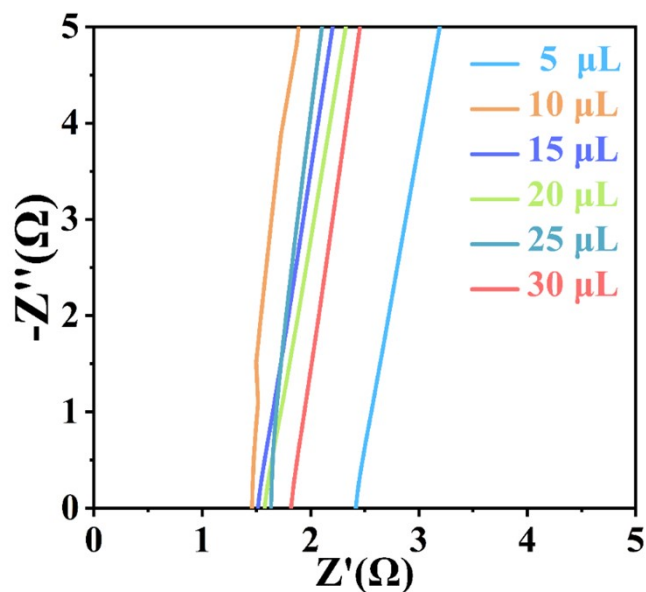
Figure S7. EIS of SS|E-PLT|SS cells batteries with different contents of 1 M LiTFSI/TEGDME.

By measuring the ionic conductivity of E-PLT electrolyte with different concentrations of 1 M LiTFSI/TEGDME, it was found that adding 10 μL of LiTFSI/TEGDME exhibited the highest ionic conductivity at room temperature (Table S2). When the liquid electrolyte content is insufficient, the electrolyte cannot be fully infiltrated, thus affecting the efficiency of ion conduction. The lower the viscosity of the electrolyte, the better the mobility of polymer segments, which is more conducive to ion conduction.[2] Increasing the LiTFSI content also increases the viscosity of the electrolyte to some extent, thereby reducing the ion conductivity.
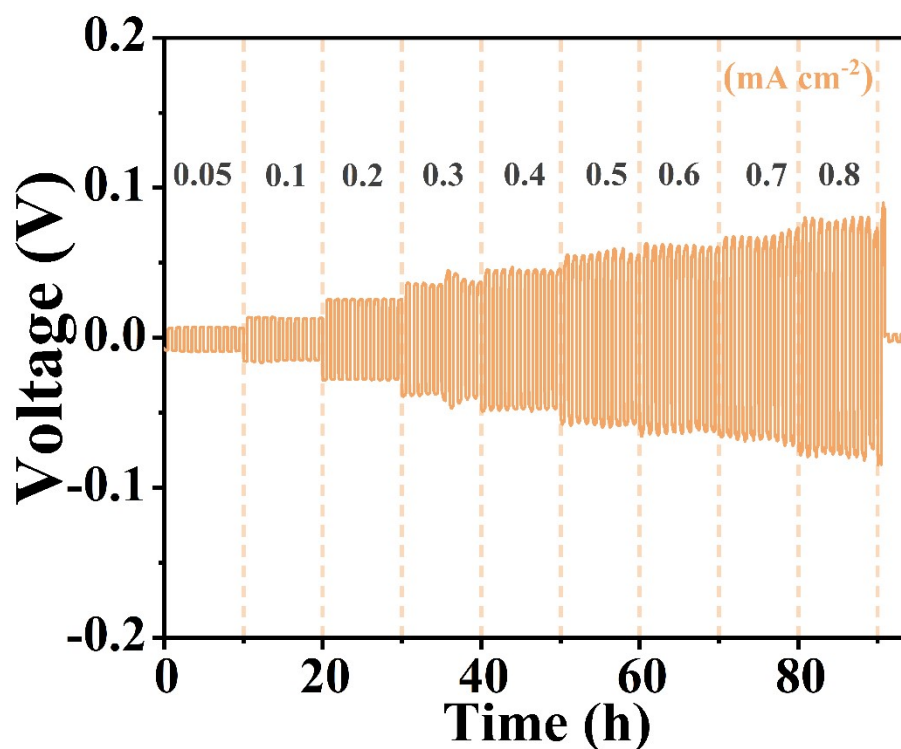
Figure S8. Galvanostatic cycling tests under step-increased current densities of Li/E-PLT/Li cells.

According to Figure S8, the critical current density (CCD) of the E-PLT electrolyte is 0.8 mA cm^{-2}. The polarization voltage of the Li/E-PLT/Li cell increases with increasing current density. Even at a current density of 0.8 mA cm^{-2}, the battery maintains stable cycling without short-circuiting. When the current density increases to 0.9 mA cm^{-2}, the growth of lithium dendrites punctures the electrolyte membrane, causing a short circuit in the battery.
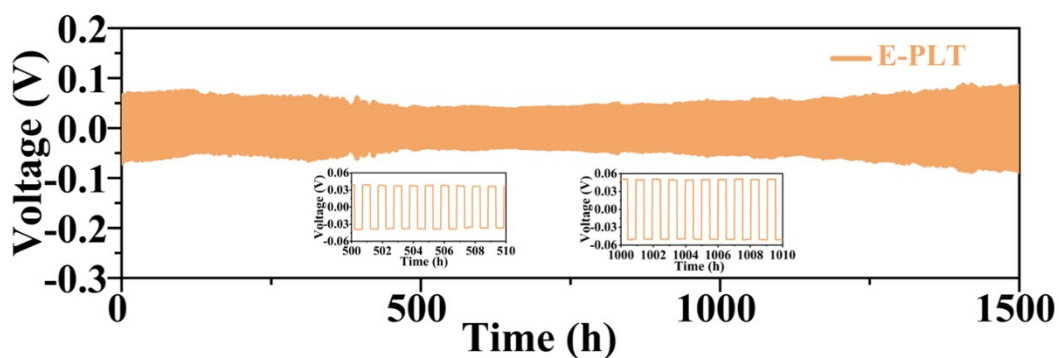
Figure S9. Galvanostatic cycling performance of Li/E-PLT/Li symmetric batteries at a current density of 0.5 mA cm^{-2}.

The Li/E-PLT/Li cell demonstrated an extended cycle life of 1500 h at a current density of 0.5 mA cm^{-2}. This phenomenon is likely due to the fibrous nature of the E-PLT electrolyte, which efficiently normalizes the Li$^+$ flux and provides effective Li$^+$ transport pathways, notable improvement over the C-PLT. Moreover, the enhanced interfacial stability at the electrode-electrolyte interface effectively curtails the growth of lithium dendrites.
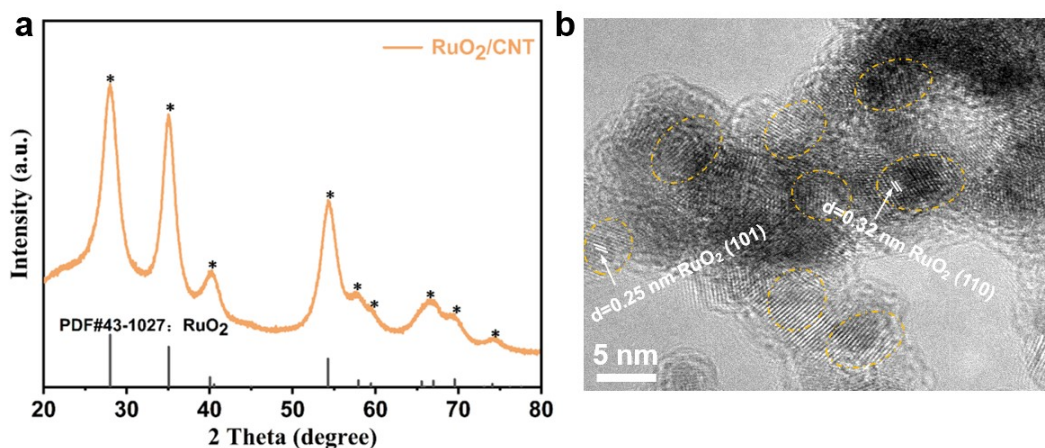

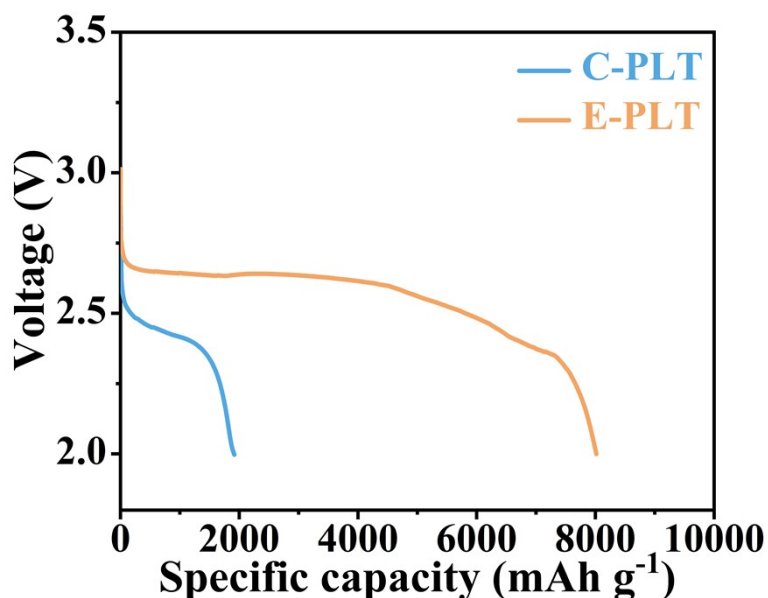**Figure S10.** (a) XRD patterns of RuO$_2$/CNT powder. (b) TEM image of pristine RuO$_2$/CNT powder.

Figure S11. Full discharge performance of the Li-O_2 batteries with different electrolytes at 200 mA g^{-1}.

Figure S11 shows the initial full discharge curves of Li-O_2 batteries with different electrolytes at a current density of 200 mA g^{-1}. The battery using E-PLT exhibits a superior initial discharge capacity (8016.5 vs 1918.5 mAh g^{-1}), the energy density of the battery is calculated to be 527.1 Wh kg^{-1} based on the cathode (8.2 mg).
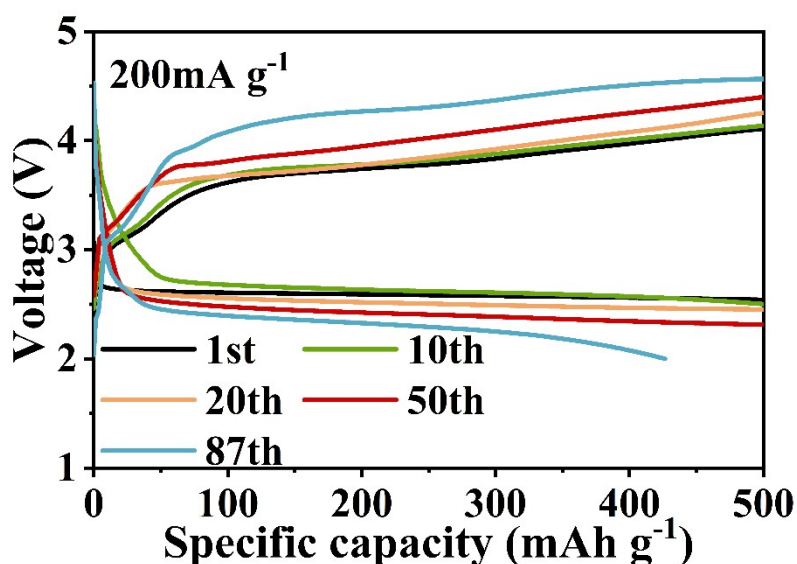

Figure S12. Discharge/charge profiles of conventional nonaqueous Li-O_2 batteries based on the ether-based liquid electrolyte (1 M LiTFSI/TEGDME, 100 µL) at a current density of 200 mA g^{-1} with a fixed capacity of 500 mAh g^{-1}.
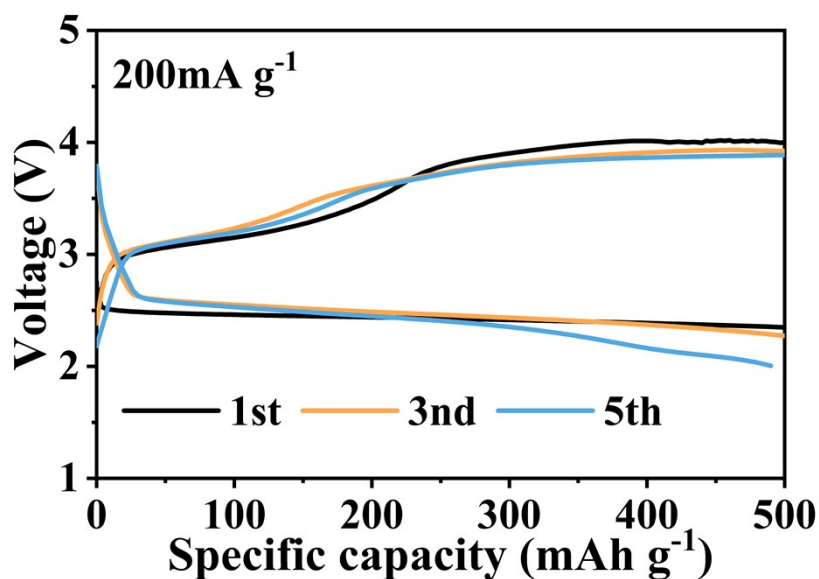
11

Figure S13. Discharge/charge profiles of Li-O_2 battery with C-PLT electrolyte at a current density of 200 mA g^{-1} with a fixed capacity of 500 mAh g^{-1}.

The Li-O_2 battery with C-PLT electrolyte showed a rapid decrease in discharge voltage, reaching cut-off voltage after 5 cycles. The observed behavior is linked to substantial rise in cell polarization caused by the unstable interface between the lithium anodes and the C-PLT membrane.
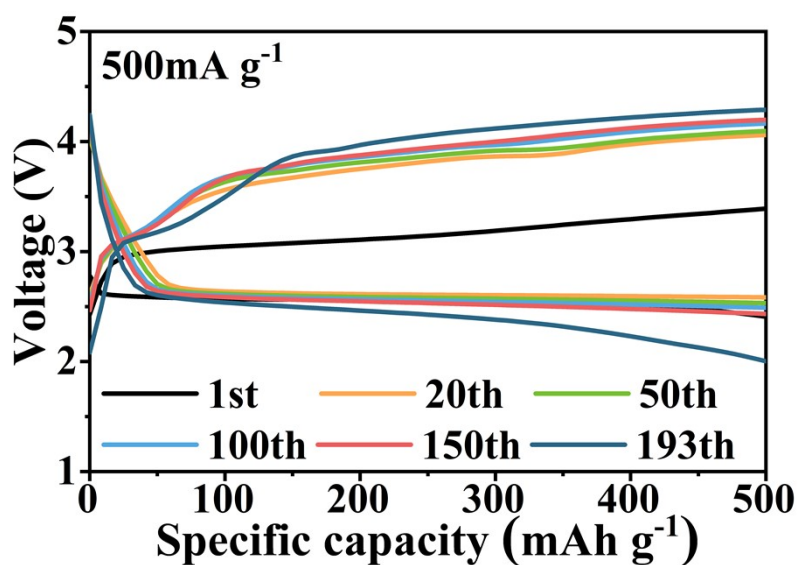

Figure S14. Discharge/charge profiles of Li-O_2 batteries with E-PLT electrolyte at a current density of 500 mA g^{-1} with a fixed capacity of 500 mAh g^{-1}.
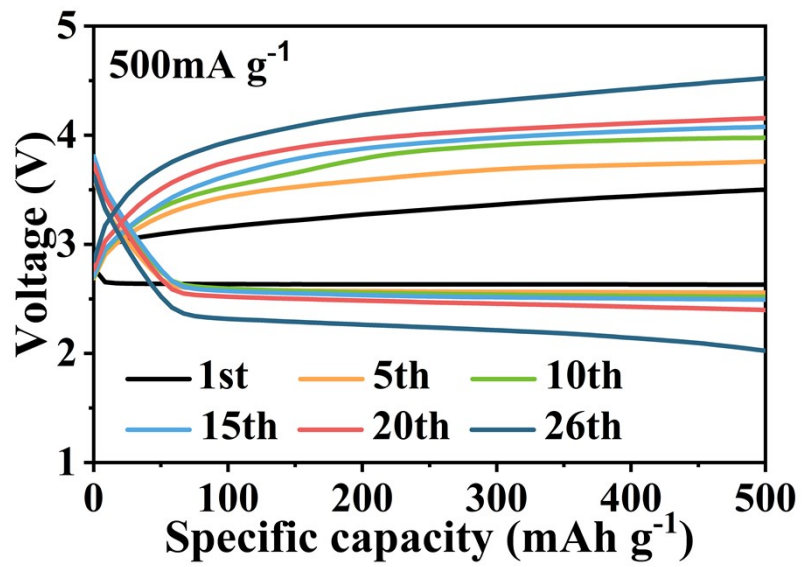
Figure S15. Discharge/charge curves of Li-O$_2$ batteries at a current density of 500 mA g^{-1} with a fixed capacity of 500 mAh g^{-1} in the air atmosphere.
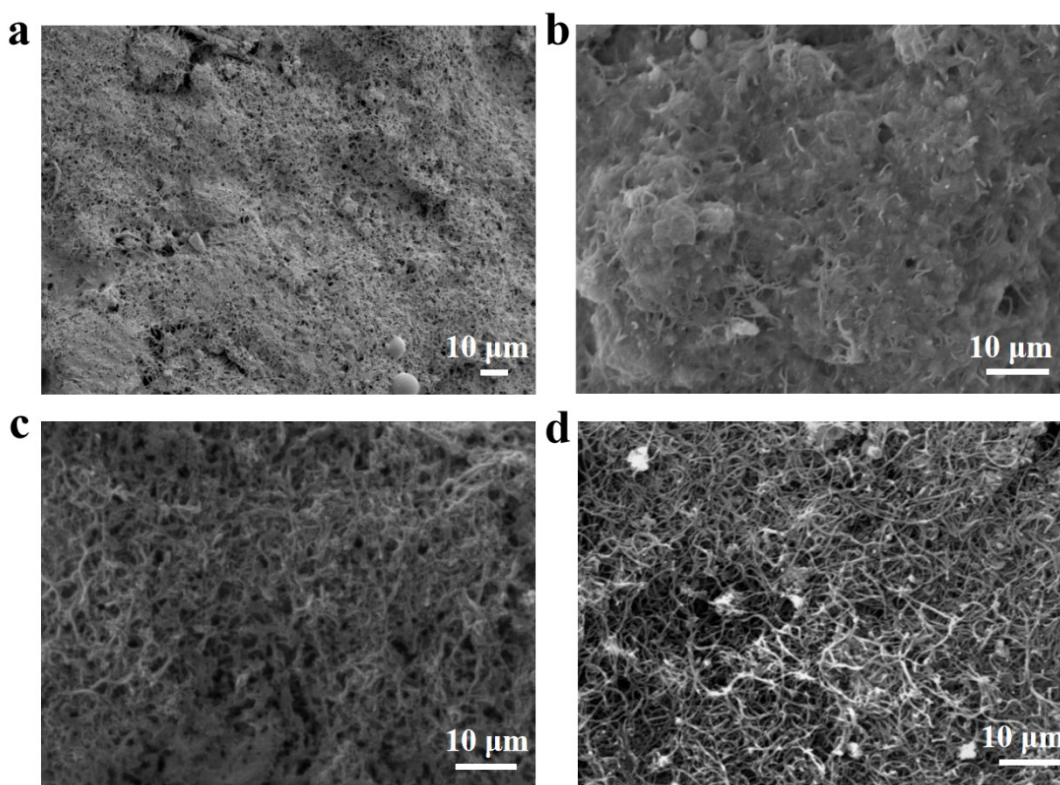
Figure S16. SEM images of the C-PLT based Li-O$_2$ batteries cathodes after first (a) discharge and (b) recharge processes. SEM images of the E-PLT based Li-O$_2$ batteries cathodes after first (c) discharge and (d) recharge processes.

The SEM images illustrate the accumulation of discharge products on the cathode surface of the C-PLT electrolyte-based SSLOBs. This accumulation persists even after the charging process, affecting the cycling performance by reducing active sites due to the buildup of discharge products. On the contrary, the cathode of SSLOBs based on E-PLT electrolyte showed that the discharge products almost disappeared after the charging process and the cathode was almost restored to its original state, indicating the reversible formation and decomposition of the discharge products.
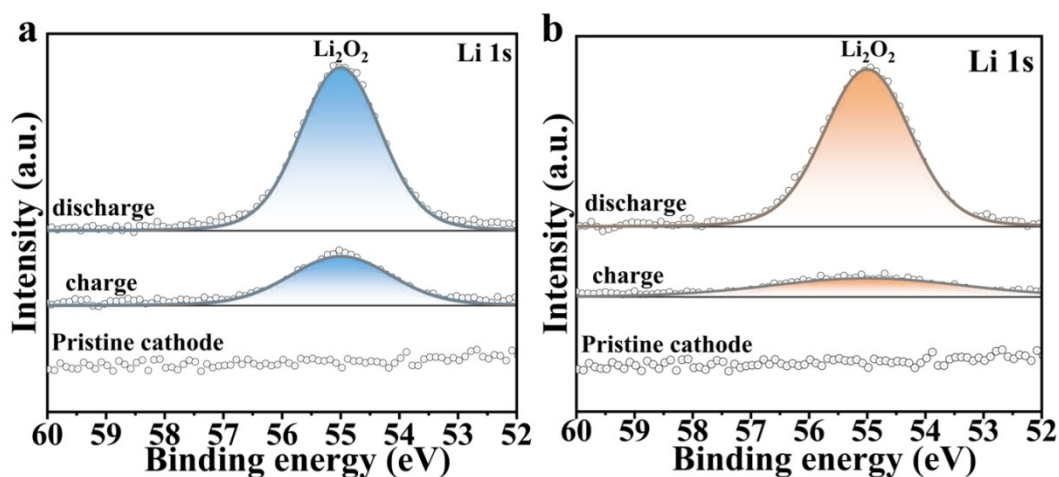
Figure S17. XPS spectra for Li 1s of the pristine, discharged, and recharged cathodes in (a) C-PLT-based and (b)E-PLT-based SSLOBs.

The composition of the discharge products was analyzed by XPS, and the E-PLT-based discharge anode has a distinct peak corresponding to Li_2O_2, and the majority of the discharge products are reversibly decomposed during charging, indicating the reversible formation and decomposition of Li_2O_2. Conversely, the cathode in C-PLT-based systems retains a significant portion of undecomposed Li_2O_2 post-charging.

Table S1. The amount of liquid absorbed in E-PAN and C-PAN electrolyte.

	E-PAN	C-PAN
Initial mass	1.5 mg	1.5 mg
Mass after soaking 12h	11.5 mg	3.9 mg
Liquid content	666.7%	160%

Table S2. The ionic conductivity of E-PLT-based batteries with varying concentrations of 1 M LiTFSI/TEGDME at room temperature.

Content (µL)	5	10	15	20	25	30
σ (mS cm^{-1})	1.02	1.67	1.64	1.57	1.52	1.36

References

1. B. Liu, W. Xu, L. Luo, J. Zheng, X. Ren, H. Wang, M. H. Engelhard, C. Wang and J. Zhang, *Adv. Energy Mater.*, 2019, **9**, 1803598.
2. X. Ma, J. Yu, Y. Hu, J. Texter and F. Yan, *Ind. Chem. Mater.*, 2023, **1**, 39–59.